

Strong coupling expansion for the Bose-Hubbard and the Jaynes-Cummings lattice model

Christoph Heil* and Wolfgang von der Linden
*Institute of Theoretical and Computational Physics,
Graz University of Technology, 8010 Graz, Austria*

(Dated: July 6, 2022)

A strong coupling expansion, based on the Kato-Bloch perturbation theory, which has recently been proposed by Eckardt et al.¹ and Teichmann et al.² is implemented in order to study various aspects of the Bose-Hubbard and the Jaynes-Cummings lattice model. The approach, which allows to generate numerically all diagrams up to a desired order in the interaction strength is generalized for disordered systems and for the Jaynes-Cummings lattice model. Results for the Bose-Hubbard and the Jaynes-Cummings lattice model will be presented and compared with results from VCA and DMRG. Our focus will be on the Mott insulator to superfluid transition.

PACS numbers: 64.70.Tg, 73.43.Nq, 11.15.Me, 03.75.HH

I. INTRODUCTION

The experimental progress in the field of ultracold atoms in periodic lattices³ allowed for a direct observation of quantum phase transitions. A very prominent example is the experiment by Greiner et al.⁴, where they observed the Mott insulator-superfluid⁵ phase transition of ultracold Rubidium atoms trapped in a three-dimensional optical lattice. This phase transition is driven by two counteracting factors. On the one hand there is a repulsive interaction between particles on the same site, trying to minimize the particle number fluctuation per site and on the other hand there is a gain of kinetic energy whenever a particle tunnels from one site to another.

If one has a condensate of ultracold atoms in a Mott insulator phase, i.e. every lattice site is occupied by the same number of particles, one can drive a phase transition to the superfluid phase, where the wave functions of the particles are no longer localized, by gradually decreasing the intensity of the lattice forming laser beams. Because of this tunability of the experimental system⁶ it provides a great testing ground for various quantum many body theories. Two such theoretical models are the Bose-Hubbard (BH) and the Jaynes-Cummings lattice (JCL) model. While the BH model considers the two different interactions of bosons explained above⁷, the JCL model takes this thought further and also factors in the interaction of bosons with a two level atomic system. It therefore constitutes a pure quantum transcription of the semi-classical Rabi model.

In this paper we are going to treat these two systems with a diagrammatic approach to the perturbation theory, as suggested by Eckardt et al.¹ and already incorporated for the ordered BH model by Teichmann et al.². We extended the approach to deal with disordered BH systems and the JCL model with additional degrees of freedom per unit cell. In addition, we give some details for an efficient numerical computation of the strong-coupling diagrams and also outline the limitations and possible pitfalls of this approach.

The paper is organized as follows: The first part deals with the BH model. In Sec. II we are going to introduce the BH model in more mathematical details. Sec. III then goes on to explain how the Kato formalism can be incorporated to calculate corrections to the ground state energy. After this introduction we are then going to discuss how this approach can be turned in numerical algorithms in Sec. IIIB.

Sec. IIIC then shows a comparison of our results with ones obtained with VCA⁸. In Sec. IV we are going to discuss the Mott insulator-superfluid phase transition, how the phase boundary can be detected and which changes we have to apply to our algorithms. Sec. IV 4 contains the results we obtained and also a discussion of the problems one encounters when trying to determine the phase boundary for a one-dimensional system with this approach. In Sec. IVA we offer a workaround for this problem and show a comparison of our data with results obtained with DMRG by Kühner et al.⁹. Sec. V explains how disordered BH systems can be treated with our approach.

In the second part of our paper we occupy ourselves with the JCL model, that is going to be put on a mathematically sound basis in Sec. VI. Sec. VIA then outlines the numerical transcription and what has to be changed in comparison to the BH implementation. Our results are shown in Sec. VIB, where we compare the energies of various systems with different occupation numbers and dimensions. Additionally we compare our data with results obtained with VCA¹⁰. The calculation of the Mott insulator-superfluid phase transition is then explained in Sec. VIC.

We conclude our paper in Sec. VII with a recapitulation of the obtained results, insights and a short outlook.

II. THE BOSE-HUBBARD MODEL

The Bose-Hubbard model is used to describe bosonic particles in a lattice at very low temperatures¹¹ and has been treated with many different methods, including the

mean-field method⁷, DMRG^{12–15}, QMC^{16–19} and strong-coupling methods^{20,21}. A particularly efficient strong coupling approach, based on the Kato-Bloch perturbation theory, has been used by Teichmann et al.². The BH hamiltonian reads

$$\hat{H} = \hat{H}_0 + \hat{H}_1 \quad (1)$$

$$\hat{H}_0 = \frac{U}{2} \sum_i \hat{n}_i(\hat{n}_i - 1) - \mu \sum_i \hat{n}_i - \sum_i \varepsilon_i \hat{n}_i \quad (2)$$

$$\hat{H}_1 = t \sum_{\langle i,j \rangle} \hat{a}_i^\dagger \hat{a}_j. \quad (3)$$

It is split into two terms, \hat{H}_0 and \hat{H}_1 , suitable for strong coupling perturbation theory. \hat{H}_0 contains three terms describing the atomic limit. In the first one, U stands for the strength of the local Coulomb interaction and \hat{n}_i is the particle number operator of site i . The second term represents the chemical potential in the grand canonical ensemble and the third contribution accounts for diagonal disorder. The perturbation part of the hamiltonian \hat{H}_1 covers the hopping processes, described by standard bosonic annihilation \hat{a}_j and creation operators \hat{a}_j^\dagger . We consider only nearest-neighbor hopping, indicated by $\langle i,j \rangle$, with hopping strength t . To begin with, we consider a homogeneous system $\varepsilon_i = 0$. Disorder can easily be accounted for in a second step as shown in Sec. V. Energies will be expressed in units of U . The eigenvectors of \hat{H}_0 are occupation-number tensor products

$$|\mathbf{n}\rangle := \bigotimes_{i=1}^N |n_i\rangle_i,$$

where the number of bosons at site x_i is given by the integer n_i . The corresponding eigenvalues are

$$\varepsilon(\mathbf{n}) := \sum_{i=1}^N n_i \left(\frac{1}{2}(n_i - 1) - \mu \right) \quad (4)$$

The ground state of \hat{H}_0 is denoted by

$$|\mathbf{g}\rangle := \otimes_i |g\rangle_i,$$

where each site is occupied by the same number of bosons, g , which is determined by minimizing $\varepsilon(\mathbf{n})$ for a given value of the chemical potential. The groundstate energy is therefor

$$\varepsilon_0 := Ng \left(\frac{1}{2}(g - 1) - \mu \right)$$

For the following discussion it is expedient to write the hopping part in a different form

$$H_1 := t \sum_b \hat{h}_b \quad (5)$$

$$\hat{h}_b = a_{b_2}^\dagger a_{b_1} \quad (6)$$

$$b \in \mathcal{P} := \{(i_2, i_1) | i_{1/2} \in \{1, 2, \dots, N\}\}.$$

where the sum runs over all directed bonds (dibonds) of nearest neighbor sites and \hat{h}_b describes the corresponding hopping process.

III. GROUND STATE ENERGY

In order to calculate the ground state energy in strong coupling perturbation theory, we make use of the Kato-Bloch formalism^{3,22–24}, which yields closed expressions for every order, in contrast to standard Schrödinger-Rayleigh perturbation theory. In the present form, the Kato-Bloch perturbation theory is only applicable to a non-degenerate ground state. The strong coupling approach is described in great detail in ref.^{1,2}. Here we summarize the key points of the formalism necessary to understand the generalization towards disordered systems and the JCL hamiltonian. In addition we will present a different perspective that allows to exploit graph theoretical techniques in order to speed up the algorithmic implementation.

The n^{th} order correction for the ground state can be written as

$$\Delta E_g^{(n)} = \sum_{\{k_\nu\}^{(n-1)}} \langle \mathbf{g} | H_1 S_{k_n} \dots H_1 S_{k_2} H_1 S_{k_1} H_1 | \mathbf{g} \rangle, \quad (7)$$

where the sum runs over all sets $\{k_\nu\}^{(n)} := \{(k_1, k_2, \dots, k_{n-1})\}$ of non-negative integers k_ν , which satisfy the following conditions

$$\begin{aligned} \sum_{l=1}^s k_l &\geq s; & \text{for } s = 1, \dots, n-2 \\ \sum_{l=1}^{n-1} k_l &= n-1. \end{aligned} \quad (8)$$

The operators S_k are diagonal in the occupation-number basis

$$\langle \mathbf{n} | S_k | \mathbf{n}' \rangle = \delta_{\mathbf{n}, \mathbf{n}'} S_k(\mathbf{n}) \quad (9)$$

$$S_k(\mathbf{n}) = \begin{cases} -\delta_{\mathbf{n}, \mathbf{g}} & \text{for } k = 0 \\ \frac{1 - \delta_{\mathbf{n}, \mathbf{g}}}{(\varepsilon_0 - \varepsilon(\mathbf{n}))^k} & \text{otherwise} \end{cases} \quad (10)$$

Eventually, the energy correction can be expressed as series in powers of the perturbation strength t

$$\Delta E_g = \sum_n \alpha^{(2n)}(g) t^n. \quad (11)$$

More details will be given in chapter IV.

A. Graphical representation

Next we will map the evaluation of Eq. (7) onto a graphical problem. For simplicity we consider simple cubic lattices in d dimensions. The generalization to other lattices is fairly straight forward. We start out from a finite cubic lattice with N lattice sites enumerated in some

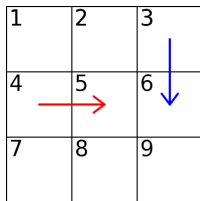


FIG. 1: Two possible hopping processes on a square lattice.

suitable way and periodic boundary conditions. Eventually the energy per site is computed for the thermodynamic limit, $N \rightarrow \infty$. We consider Eq. (7) for a specific order n and sequence $\{k_\nu\}^{(n)}$. From the n factors H_1 we obtain a multiple sum over dibonds

$$\begin{aligned} & \langle \mathbf{g} | H_1 S_{k_{n-1}} \dots H_1 S_{k_1} H_1 | \mathbf{g} \rangle \\ &= t^n \sum_{b^{(1)}, \dots, b^{(n)}} \langle \mathbf{g} | \hat{h}_{b^{(n)}} S_{k_{n-1}} \dots \hat{h}_{b^{(2)}} S_{k_1} \hat{h}_{b^{(1)}} | \mathbf{g} \rangle . \end{aligned} \quad (12)$$

There are two important aspects. Firstly, the application of any of the dibond hopping operators h_b on an occupation-number basis vector results in just another such basis vector

$$h_b |\mathbf{n}\rangle = |\mathbf{n}'\rangle .$$

Secondly, the operators S_k are diagonal in the occupation number basis and they merely introduce weight factors. Hence, the index τ of the dibond operators $h_{b^{(\tau)}}$ defines an auxiliary time and $b^{(\tau)}$ can be any of the $2d$ dibonds on the d -dimensional simple cubic lattice. Each of the individual dibond hopping processes can be depicted as a directed line (vector) on the underlying lattice, connecting neighboring sites. An example is given in Fig. 1, where the dibond hopping terms $\hat{a}_5^\dagger \hat{a}_4$ and $\hat{a}_6^\dagger \hat{a}_3$ are represented as arrows. The resulting pattern of arrows can be considered as a labelled digraph²⁵. So far, the sum over dibonds in Eq. (12) can be replaced by a sum over all labelled digraphs \mathcal{G} , consisting of directed nearest neighbor lines. Such a digraph covers a certain set of lattice sites, which in ordered form be

$$i_1 < i_2 < \dots < i_m ,$$

where m is the number of vertices of the digraph. Due to the homogeneity of the lattice we can renumber the lattice sites in sequential order without changing the resulting matrix elements in Eq. (12).

$$i_\nu \rightarrow \nu ; \quad \nu = 1, \dots, m .$$

The digraph defines a set $\mathcal{B} = \{b^{(i)}\}$ of dibonds, but not the order in which they occur in Eq. (12). Therefore, in addition to the sum over all digraphs \mathcal{G} with n directed lines, we have to sum over all distinct sequences of dibond operators occurring in \mathcal{G} . Obviously, multiple dibonds are indistinguishable and need not be permuted. For

each dibond sequence \vec{b} , we compute the corresponding matrix elements (weights of the digraph)

$$\begin{aligned} w(\mathcal{G}) &= \langle \mathbf{g} | \hat{h}_{b^{(n)}} S_{k_{n-1}} \dots \hat{h}_{b^{(2)}} S_{k_1} \hat{h}_{b^{(1)}} | \mathbf{g} \rangle \\ &= \langle g_1, \dots, g_m | \hat{h}_{b^{(n)}} S_{k_{n-1}} \dots \hat{h}_{b^{(2)}} S_{k_1} \hat{h}_{b^{(1)}} | g_1, \dots, g_m \rangle , \end{aligned} \quad (13)$$

where, due to the tensor structure of the vectors and the structure of the operators, only the sites $1, \dots, m$ are involved. An immediate consequence is that the weight of all isomorphic digraphs is the same. Since the computation of the matrix elements is the most cpu-time consuming step, it is expedient to represent the digraphs by topologically different members and the corresponding multiplicity.

1. Translational invariance

One class of isomorphism is due to translational invariance. Each digraph, apart from the lattice-site labels, occurs in N copies on the lattice with periodic boundary conditions, which results in an overall factor N . In order to avoid the computation of N identical contributions, we compute the energy per site, by restricting the sum over all digraphs to those attached to the origin. Graphs attached to the origin shall be defined by the condition

$$\min_i \bar{x}^{(i)} = \vec{0} , \quad (14)$$

where $\bar{x}^{(i)}$ is the position of the i -th site on the underlying lattice, covered by the digraph.

2. Additional constraints on the graphs

Yet not all digraphs contribute to the energy. There are two constraints for non-zero contributions. Firstly, the number of dibonds entering a site has to balance the number of dibonds leaving it (*local particle conservation rule*). Otherwise, the number of bosons at that site would have changed due to the hopping processes and the groundstate expectation value is zero. In graph-theory language the digraph is said to be balanced and consequently it has no sources or sinks, i.e. sites with only one dibond attached to it. We call the admissible digraphs shortly *particle conserving*. In Fig. 2 the left graph is admissible/particle conserving while the right one is not.

A second constraint is due to the linked cluster theorem. As shown in ref.^{1,2} and references therein, contributions of disconnected graphs cancel. A simple argument is given by the extensivity of the energy, i.e. it has to be proportional to N . Disconnected graphs yield higher orders in N , since each disconnected part can be placed roughly speaking on N different sites.

In summary, admissible digraphs are connected and balanced. From graph theory it is known²⁵ that such



(a) in-degree = out-degree (b) not sink- and source-free.

FIG. 2: Examples of closed (a) and open(b) paths in second order.

graphs are Eulerian, i.e. they can be traversed along the directed lines by visiting each directed line exactly once. This very feature will be used to generate all digraphs.

Examples of several low-order diagrams are given in ref.^{1,2}.

B. Algorithm

Here we give an algorithm to generate the, topologically different, connected and balanced digraphs on a simple cubic lattice.

1. Generation of topologically different digraphs

We start at the origin of the lattice and generate an Eulerian circuit of length n by tracing a tour sequentially to neighboring sites. At every site there are $2d$ choices to proceed. The problem is equivalent to searching in trees. We apply a depth-first search algorithm up to depth n . If we reach the origin at that point, the corresponding path is shifted such that it fulfills Eq. (14) and is added to a list. Multiple entries of the same path are discarded. The same path can occur several times, as we can consider any site of the path as origin, from which the path is initiated. This multiplicity is an artifact of the algorithm and has to be eliminated.

Next we need to identify topologically different digraphs. Digraphs are isomorphic if and only if for some ordering of their vertices, their adjacency matrices are equal. Let

$$\{i_1, i_2, \dots, i_{n+1}\}$$

be the sequence of site-indices encountered during the tour. The number of different sites (vertices) be m . By construction and as demanded for balanced digraphs, all indices $1, 2, \dots, L$ occur at least twice in the sequence. The adjacency matrix can be computed by

$$A_{i,j} = \sum_{l=1}^n \delta_{i,i_l} \delta_{j,i_{l+1}},$$

and $A_{i,j}$ is the number of times the path goes from site i to site j or in other words, the number of dibonds from site i to site j .

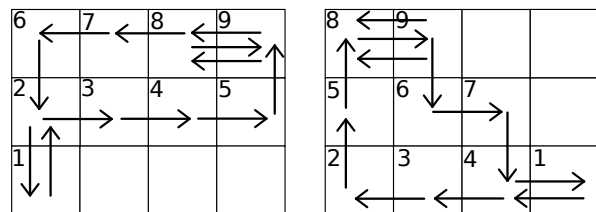


FIG. 3: Two identical digraphs of order $n = 12$. The generating paths are attached to the origin.

Two digraphs are isomorphic if and only if the corresponding matrices are similar

$$M' = PMP^{-1}.$$

with P being a permutation matrix. Provided two graphs are isomorphic, trace and determinant of M' and M'' for any integer power ν have to agree. This can be used as a quick tests to rule out isomorphism. A representative example of two digraphs that pass all these tests is depicted in Fig. 3. The corresponding adjacency matrix of the left digraph is

$$M_1 = \begin{pmatrix} 0 & 1 & 0 & 0 & 0 & 0 & 0 & 0 & 0 \\ 1 & 0 & 1 & 0 & 0 & 0 & 0 & 0 & 0 \\ 0 & 0 & 0 & 1 & 0 & 0 & 0 & 0 & 0 \\ 0 & 0 & 0 & 0 & 1 & 0 & 0 & 0 & 0 \\ 0 & 0 & 0 & 0 & 0 & 0 & 0 & 0 & 1 \\ 0 & 1 & 0 & 0 & 0 & 0 & 0 & 0 & 0 \\ 0 & 0 & 0 & 0 & 0 & 1 & 0 & 0 & 0 \\ 0 & 0 & 0 & 0 & 0 & 0 & 1 & 0 & 1 \\ 0 & 0 & 0 & 0 & 0 & 0 & 0 & 2 & 0 \end{pmatrix} \quad (15)$$

and the adjacency matrix of the right digraph reads

$$M_2 = \begin{pmatrix} 0 & 1 & 0 & 0 & 0 & 0 & 0 & 0 & 0 \\ 1 & 0 & 1 & 0 & 0 & 0 & 0 & 0 & 0 \\ 0 & 0 & 0 & 1 & 0 & 0 & 0 & 0 & 0 \\ 0 & 0 & 0 & 0 & 1 & 0 & 0 & 0 & 0 \\ 0 & 0 & 0 & 0 & 0 & 0 & 0 & 0 & 1 \\ 0 & 1 & 0 & 0 & 0 & 0 & 0 & 0 & 0 \\ 0 & 0 & 0 & 0 & 0 & 1 & 0 & 0 & 0 \\ 0 & 0 & 0 & 0 & 0 & 0 & 1 & 0 & 1 \\ 0 & 0 & 0 & 0 & 0 & 0 & 0 & 2 & 0 \end{pmatrix} \quad (16)$$

At first glance, the two matrices seem to be different, but the distinction stems from the labeling. If we denote by P the matrix associated with the permutation

$$((1), (2, 4), (3), (5), (6, 7), (8, 9)),$$

then we can easily verify the similarity of M_1 and M_2

$$M_2 = P^{-1}M_1P.$$

The algorithm generates a list of unlabeled (topologically different) digraphs, along with their multiplicities.

An example is given in Fig. 4, where all connected and balanced digraphs with 4 directed lines, necessary for 4^{th}

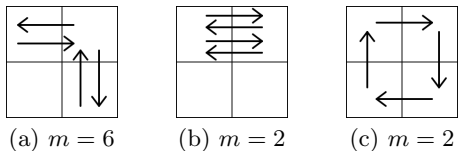


FIG. 4: All connected and balanced digraphs with 4 lines along with their multiplicities m .

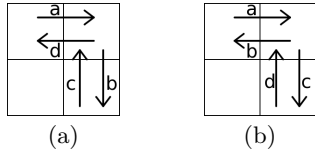


FIG. 5: Two possible time resolved dibond sequences of the digraph in Fig. 4(a).

order energy correction, are depicted along with their multiplicities.

We call a digraph reducible, if it is possible to split the dibonds into two or more subsets that represent connected and balanced subgraphs. In Fig. 4 the digraphs (a) and (b) are reducible, while (c) is not.

2. Computation of the energy correction

In order to evaluate the energy correction per site of Eq. (7) we have to go through all digraphs in the list, compute their contribution to the matrix element and multiply it by the multiplicity. The contribution of one digraph is determined in the following way. The digraph \mathcal{G} defines a set of dibond operators. We attach auxiliary times $\tau = 1, \dots, n$ to the dibond operators in all possible but distinguishable ways. Each time sequence $(b^{(n)}, \dots, b^{(1)})$ defines an additive contribution to Eq. (7). Fig. 5 shows two different time dependent dibond sequences for the same digraph of Fig. 4(a). We still have to account for the sum over the Kato-Bloch indices $\{k_\nu\}^{(n)}$. To this end, we analyze the sequence $(b^{(n)}, b^{(n-1)}, \dots, b^{(1)})$ in more detail. It may happen, that at time τ , the subsequence $(b^{(\tau)}, b^{(\tau-1)}, \dots, b^{(1)})$ forms already a connected and balanced sub-digraph $\mathcal{G}^{(\tau)}$, which is equivalent to

$$\prod_{l=\tau}^1 h_{b^{(l)}} |\mathbf{g}\rangle = |\mathbf{n}\rangle. \quad (17)$$

In other words, at that time τ (there may be more than one in the entire dibond sequence) k_τ has to be 0, or rather $S_{k_\tau} = -1$. This constrains the possible Kato-Bloch indices $\{k_\nu\}^n$ defined by the condition Eq. (8). There is an additional, implicit condition due to the fact that

$$\langle \mathbf{g} | h_b | \mathbf{g} \rangle = 0 \quad (18)$$

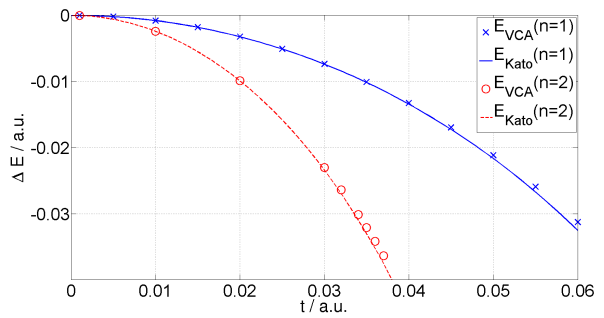


FIG. 6: Energy corrections with the present approach (up to 8th order) for 1 dimension and filling factors $g = 1$ and $g = 2$ compared with results obtained with VCA⁸.

for every dibond operator. Consequently, $k_1 \neq 0$ and $k_{n-1} \neq 0$ and for the same reason, consecutive k -values cannot be zero simultaneously, i.e. $k_i k_{i+1} \neq 0$.

3. Summary of the algorithm

- *generation of paths*: First we generate all closed paths of a given length/order n , beginning at the origin.
- *translational invariance*: Each path is attached to the origin as defined by Eq. (14). Multiple occurrences of the same path are eliminated.
- *digraphs*: The paths are translated into digraphs. Site labels are omitted and (topologically) identical digraphs are stored along with their multiplicities.
- *dibond sequences*: For each digraph, all distinct time dependent dibond sequences are generated.
- *Kato-Bloch summation*: For each dibond sequence, the compatible Kato-Bloch indices $\{k_\nu\}^{(n)}$ are determined and the contribution to the energy correction Eq. (7) are computed. Care is taken when admissible subgraphs occur.

C. Testresult

In order to test the numerical algorithm we compare the ground state energy as a function of the hopping strength for the one dimensional BH model with the results obtained by VCA⁸ in Fig. 6. The results are in very good agreement. More results for the BH model obtained with the present strong-coupling approach can be found in ref.².

IV. MOTT INSULATOR-SUPERFLUID PHASE TRANSITION

Next we will address the phase boundary between the Mott insulator and the superfluid phase. It can easily be computed in the frame of the strong-coupling Kato-Bloch formalism. There are essentially two approaches, for fixed μ or for fixed t . The latter is driven by charge fluctuations and it has been proposed to detect this boundary by computing the energy $\Delta E_g^{\pm 1}$ it takes to add or subtract a 'defect' particle²⁰. At the phase boundary, this $\Delta E_g^{\pm 1}$ vanishes (see Eq. (24) and Sec. IV A).

At fixed μ and density, the transition is driven by phase fluctuations. To detect this transition, we introduce an 'Effective Potential'^{26,27}.

1. Phase Boundary Criterion

In order to describe the superfluid phase, we add a source and a drain term to the BH hamiltonian

$$\tilde{H} = \underbrace{\hat{H}_0 + \hat{H}_{hop}}_{H_{BH}} + \sum_i \left(\eta^* \hat{a}_i + \eta \hat{a}_i^\dagger \right),$$

where η is the strength enforcing particle number fluctuations. The expansion of the grand canonical potential per site in powers of η and η^* has the general form

$$f(\eta, \eta^*) = f_0 + \sum_{l=1}^{\infty} c_{2l} |\eta|^{2l}. \quad (19)$$

For $T = 0$, the grand canonical potential can again be determined in the strong-coupling Kato-Block formalism, which allows to compute the coefficients c_{2n} that appear in equation (19) by the following power series in the hopping parameter t :

$$c_{2l} = \sum_{n=0}^{\infty} \alpha_{2l}^{(n)} t^n \quad (20)$$

The order parameter $\psi = \langle \hat{a}_i \rangle_\eta$ can be determined by

$$\psi = \frac{\partial}{\partial \eta^*} f(\eta) = (c_2 + 2c_4 |\eta|^2 + O(|\eta|^4)) \eta. \quad (21)$$

As pointed out in ref.², c_2 can be considered as a susceptibility

$$c_2 = \left(\frac{\partial \Psi}{\partial \eta} \right) \Big|_{\eta \rightarrow 0}$$

of the system to develop an order parameter driven by the source-and-drain term of strength η . Hence, the Mott-to-superfluid phase transition occurs at those points in the $\mu - t -$ phase diagram, where c_2 diverges.

The convergence radius of the power series of the function $\alpha_2^{(\nu)}(t)$ in Eq. (20) is according to d'Alembert's law (see for example ref.²⁸) given by

$$t^* = \lim_{\nu \rightarrow \infty} \left| \frac{\alpha_2^{(\nu-1)}}{\alpha_2^{(\nu)}} \right|. \quad (22)$$

In other words, the series converges if $t < t^*$ and it diverges for $t > t^*$. For given chemical potential, t^* marks the transition from the Mott insulator to the superfluid phase.

The strong coupling Kato-Bloch formalism can be applied with a modified perturbation term

$$H'_1 = H_1 + \sum_i \left(\eta^* \hat{a}_i + \eta \hat{a}_i^\dagger \right).$$

In analogy to Eq. (7) and Eq. (12) we have

$$\alpha_2^{(n-2)} = \sum_{\{k_\nu\}^{(n)}} \sum_{b^{(1)}, \dots, b^{(n)}} \langle \mathbf{g} | \hat{o}^{(n)} S_{k_{n-1}} \dots \hat{o}^{(2)} S_{k_1} \hat{o}^{(1)} | \mathbf{g} \rangle. \quad (23)$$

The operators $\hat{o}^{(\tau)}$ are either dibond operators $h_{b^{(\tau)}}$ as in Eq. (3) or individual particle creation \hat{a}_i^\dagger or annihilation operators \hat{a}_i at site i . As a matter of fact, since we are only interested in the term c_2 , exactly one creation and one annihilation operator has to be present.

2. Graphical representation

The energy contributions can again be represented graphically. For the n^{th} order contribution ($\alpha_2^{(n)}$) the graphical elements are n nearest neighbor directed lines, one source term (represented in Fig. 7 by \times) and one drain term (symbolized by \bullet in Fig. 7).

By virtue of the linked cluster theorem the graph has to be connected and the source and drain symbols are located on the vertices of the graph. On top of that, particle conservation demands

$$d^+(v_i) - d^-(v_i) = N^+(v_i) - N^-(v_i),$$

where $d^{+/-}(v_i)$ are out-/in-degrees of vertex v_i and $N^{+/-}(v_i)$ is the number of source-/drain-symbols of vertex v_i . In other words, vertices with no source/drain symbol or with a source-drain pair are balanced, while a vertex with only a source (drain) symbol has to have one spare outgoing (incoming) directed line.

3. Construction of admissible digraphs

The admissible digraphs can easily be completed to form a balanced connected digraph, by adding an extra *bath site*, from which a directed line goes to the source

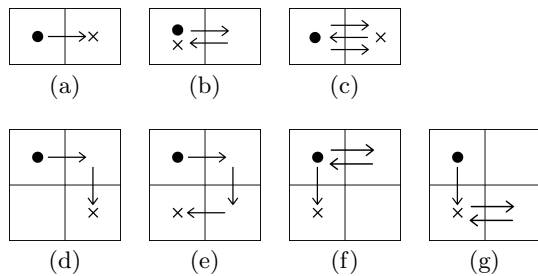


FIG. 7: All paths up to third order with one source (solid circle), and one drain (\times), that have a non-vanishing contribution.

TABLE I: Number of topologically different digraphs for given order and dimension

| order | 1-dim | 2-dim | 3-dim |
|-------|-------|-------|-------|
| 1 | 1 | 1 | 1 |
| 2 | 2 | 2 | 2 |
| 3 | 4 | 4 | 4 |
| 4 | 8 | 10 | 10 |
| 5 | 14 | 22 | 22 |
| 6 | 25 | 58 | 58 |
| 7 | 45 | 140 | 140 |
| 8 | 79 | 390 | 394 |

symbol and to which a directed line enters from the drain symbol. This is not necessarily a nearest neighbor line and can even be a self-loop. The sought-for digraphs are therefore Eulerian and can be constructed by tracing a continuous tour. The tour begins at the origin with a source symbol (\bullet) and proceeds successively along nearest neighbor dibonds. For the n^{th} order term $\alpha_2^{(n)}$ we generate n directed lines and close the graph with a drain symbol (\times). This time, it is not compulsory that the tour forms a closed path. Eventually, the digraph is attached to the origin according to Eq. (14). As before, multiple copies of the same digraph (which are an artifact of the algorithm) are discarded.

The expectation value in Eq. (23) is invariant against relabeling the sites, i.e. isomorphic digraphs yield the same contribution to $\alpha_2^{(n)}$. We again identify isomorphism by similar adjacency matrices.

In Fig. 7 all topologically different admissible digraphs to compute $\alpha_2^{(n)}$ up to order $n = 3$ are depicted.

In addition, table I shows the number of topologically unique diagrams as a function of the order ν for systems with 1, 2 and 3 dimensions.

As before, we have to sum over all distinguishable time-sequences of the elements in the digraphs, which are this time n dibond hopping terms and one creation and one annihilation operator. In the worst case the sum runs over $(n + 2)!$ terms, if all dibonds are different.

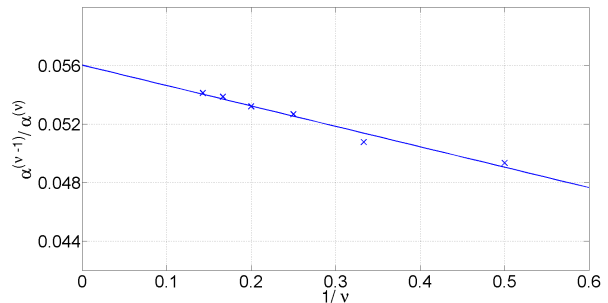


FIG. 8: The ratios $|\alpha_2^{(\nu-1)}/\alpha_2^{(\nu)}|$ as function of $1/\nu$ and extrapolated to $\nu \rightarrow \infty$ using a linear fit for the first Mott lobe ($g = 1$) for a 2d system with $\mu/U = 0.3$.

We can use Eq. (22) to determine the phase boundary between the Mott insulator and the superfluid phase. For a fixed value of the chemical potential, the convergence radius t^* defines the hopping strength t at which the transition takes place. If the phase boundary $t^*(\mu)$ is not unique, like in the 1d case, where a reentrance into the Mott phase occurs, the convergence radius would yield the smallest value for the phase boundary, where as in 2d and 3d the phase boundary as a function of t for fixed μ is unique. However, in the 1d case, there is an even more severe reason why the present procedure fails, which will be explained in Sec. IV A

Following Eq. (22), we calculate the ratio $|\alpha_2^{(\nu-1)}/\alpha_2^{(\nu)}|$ and plot it as function of $1/\nu$. The extrapolation $\frac{1}{\nu} \rightarrow 0$ yields the sought-for value of the phase boundary. In Fig. 8 a representative example is depicted. Further details and examples can be found in ref.^{1,2}

4. Testresults

The phase diagram for the BH model has already been computed with high accuracy by various techniques as well as by the strong-coupling Kato-Bloch approach by Teichmann et al.^{2,29}. Our results agree very well with those results. A typical set of data can be seen in Fig. 9, where results are also presented for the 3d case.

While the 2d results agree remarkably well with results from other methods³⁰, the 1d case causes some problems close to the tip of the Mott lobe. In Fig. 10 we compare our results with those of DMRG⁹. Teichmann et al.^{2,29} already pointed out that the strong-coupling Kato-Bloch approach has some problems in detecting the phase boundary in 1d. They put the blame on the reentrance feature of the Mott lobe. For a given chemical potential, the criterion based on the radius of convergence in Eq. (22) can only provide the phase boundary with the smallest t^* . We observe however, that deviations also occur for values of the chemical potential, where there is no reentrance feature. The agreement with the DMRG results is very good for small values of t , but close to the tip deviations start to grow.

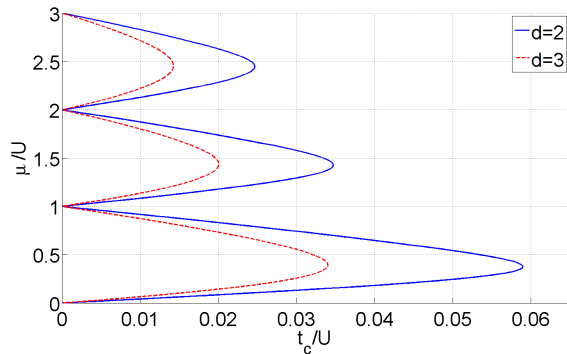


FIG. 9: The Mott insulator-superfluid phase boundary for systems with two and three dimensions and with filling factors $g = 1$, $g = 2$ and $g = 3$.

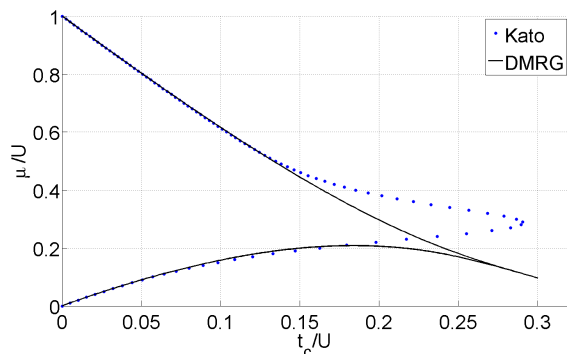


FIG. 10: Comparison of the results obtained with the Kato approach using the method of effective potential and DMRG from Kühner et al.⁹ for a 1-dimensional system with filling factor $g = 1$.

The reason is the fact that at the tip of the Mott lobe there is a Kosterlitz-Thouless (KT) transition with only a power-law decay of the correlation functions.

A. Method for 1-dimensional systems

As pointed out in the previous section, the power-law behaviour of the KT transition causes problems for the method of the effective potential. We therefore incorporated another approach that allows us to determine the phase boundary for 1d systems, proposed by Freericks et al.²⁰.

The idea is to introduce defect states, i.e. one adds/removes one particle from the Mott ground state $|\mathbf{g}\rangle \rightarrow |\dots, g_{i-1}, g_i \pm 1, g_{i+1}, \dots\rangle$. With the assumption, that the compressibility approaches zero continuously at the phase boundary, the critical chemical potential μ^* can be deduced at the point where

$$\Delta E_g^{\pm 1} = \Delta E_g^{N \pm 1} - \Delta E_g^N = 0 \quad (24)$$

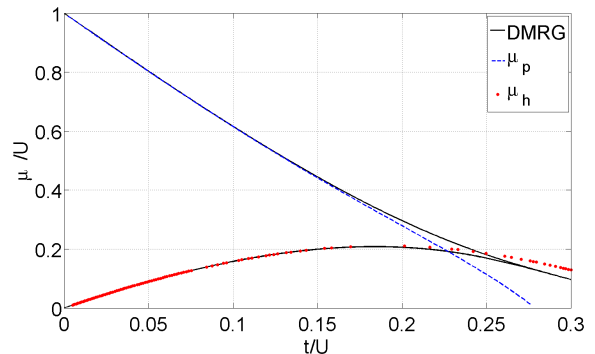


FIG. 11: Comparison of the results obtained with the Kato approach and DMRG from Kühner et al.⁹ for a 1-dimensional system with filling factor $g = 1$.

This puts us in the advantageous situation that we can now use our energy algorithm from before, which has the benefit of being immensely faster. In contrast to the method of effective potential, we now have to consider only closed paths as in Sec. III. The computation time can therefore be reduced by a considerable amount. Additionally, instead of having to calculate the critical t^* for any μ of interest separately, we only have to compute ΔE once for every particle (hole) band and can deduce from this all μ^* with a simple numerical operation. The results of such a calculation are depicted in Fig. 11.

The precise procedure works as follows. We start with the already well known Mott insulator ground state $|\mathbf{g}\rangle$. Then we add/remove one particle at the site of the origin of the considered path (We shall from now on refer to this new ground state as $|\mathbf{p}(\mathbf{h})\rangle$). Now we let this particle/hole hop through the lattice according to the diagram and all unique permutations of it. One has to pay attention to the fact, that the system for a given diagram with N_d involved sites is N_d -times degenerate²⁴. In other words, the state $|g \pm 1, g, g\rangle$ leads to the same unperturbed energy ε_0 as the states $|g, g \pm 1, g\rangle$ and $|g, g, g \pm 1\rangle$.

Consequently, all Kato sequences that include a factor $\langle \mathbf{p}(\mathbf{h}) | \hat{h}_b | \mathbf{p}(\mathbf{h}) \rangle$ can indeed have a nonvanishing contribution in contrast to the case of a non-degenerate system with only one ground state. Apart from this detail, everything works the same as explained in Sec. III.

Fig. 11 is a comparison of our results calculated up to 9th order with data from Kühner et al.⁹. As one can see, our results match those from DMRG quite well, but deviate discernably for larger t , especially in the particle band case.

This is due to the fact, that the power series expansion of μ^* with which we end up, has an asymptotic behaviour. Calculating higher orders of the perturbation series in order to improve accuracy is therefore not feasible. Hence we are going another route and do the following: We start with the power series for μ_p^* for the particle case (the hole case can be treated analogously), which we get

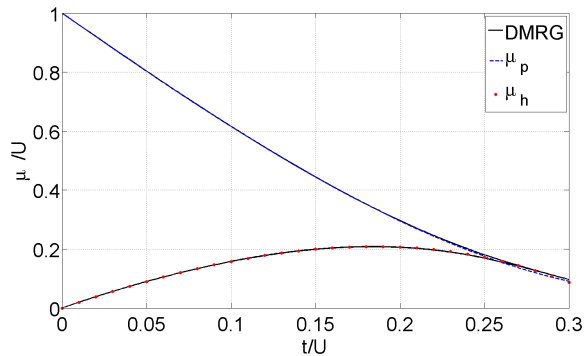


FIG. 12: Comparison of our results up to 9th order obtained with the Kato approach and DMRG from Kühner et al.⁹ for a 1-dimensional system with filling factor $g = 1$.

from the Kato-Bloch energy calculations

$$\mu_p^*(t) = \sum_{\nu=0}^{\nu_{max}} c_p(\nu) t^\nu \quad (25)$$

and perform a Borel transformation (see for example ref.³¹)

$$\mathcal{B}(z) = \sum_{\nu=0}^{\nu_{max}} c_p(\nu) \frac{z^\nu}{\nu!} . \quad (26)$$

This Borel transform now gets rewritten and approximated according to Padé³² in order to cope with the asymptotic series.

$$\mathcal{B}(z) = \frac{\sum_{m=0}^{\nu_{max}} a_m x^m}{1 + \sum_{n=1}^{\nu_{max}} b_n x^n} = \sum_{\nu=0}^{\nu_{max}} \zeta_\nu z^\nu . \quad (27)$$

The final series for $\tilde{\mu}_p^*(t)$ is then recovered by performing the integral

$$\tilde{\mu}_p^*(t) = \int_0^\infty \mathcal{B}(zt) e^{-z} dz \quad (28)$$

This revised expression for $\tilde{\mu}_p^*$ is very good natured and our results now agree excellently compared with those from the literature⁹, as can be seen in Fig. 12.

V. LOCAL DISORDER

Next we will treat local disorder, described by the last term in Eq. (2), where ϵ_i is a random variable. Local disorder can easily be incorporated into the strong-coupling Kato-Bloch formalism. The central quantity is the grand canonical potential at zero temperature, or rather the

lowest energy in Fock space for a given chemical potential, averaged over disorder realizations.

$$\langle E \rangle_\epsilon := \int E(\epsilon) p(\epsilon) d^N \epsilon ,$$

where $E(\epsilon)$ is the lowest grand canonical energy for a given disorder realization vector ϵ and $p(\epsilon)$ is the joint probability density function (pdf) for the random disorder variables. The latter are assumed to be uncorrelated and the joint pdf is the product of independent and identically distributed (iid) random variables

$$p(\epsilon) = \prod_{i=1}^N p(\epsilon_i) .$$

The n^{th} order contribution to the mean energy is according to Eq. (7)

$$\langle \Delta E_g^{(n)} \rangle_\epsilon = \sum_{\{k_\nu\}^{(n)}} \langle \langle \mathbf{g}^\epsilon | H_1 S_{k_{n-1}}^\epsilon \dots S_{k_1}^\epsilon H_1 | \mathbf{g}^\epsilon \rangle \rangle_\epsilon , \quad (29)$$

where the ground state occupation \mathbf{g}^ϵ depends on the disorder realization and will be site dependent. The same holds for the energies in the atomic limit $E^\epsilon(n)$, entering the operators S_k^ϵ . The summation over all dibond sequences in Eq. (12) is again mapped into a sum over all connected and balanced labelled digraphs. Similar to Eq. (13), the weight for one digraph \mathcal{G} is given by

$$w(\mathcal{G}) = \langle \langle g_1^{\epsilon_1}, \dots, g_m^{\epsilon_m} | \hat{h}_{b(n)} S_{k_{n-1}}^\epsilon \dots \hat{h}_{b(2)} S_{k_1}^\epsilon \hat{h}_{b(1)} | g_1^{\epsilon_1}, \dots, g_m^{\epsilon_m} \rangle \rangle_\epsilon \quad (30)$$

where only the disorder energies of the site reached by the graph are required. The mean weight is again independent of the labeling and hence isomorphic digraphs yield the same contribution. So the algorithm is almost the same as before in the homogeneous system. We generate all topological different connected and balanced digraphs along with their multiplicities. For each digraph all distinct permutations of the dibonds are generated and the summation over possible Kato-Bloch sequences is performed.

Now comes the modification: For one specific dibond sequence and one set of Kato-Bloch indices, the averages over the disorder realizations on the m involved sites has to be carried out. The same modification hold for the computation of the susceptibility α_2^n .

In order to compare with ref.⁸, we have chosen a binary disorder with $\epsilon_i = \pm\epsilon$, with disorder strength ϵ .

1. Results

Fig. 13 contains the energy for a 1-dimensional system as function of the hopping parameter for different disorder parameters ϵ as well as a comparison with results

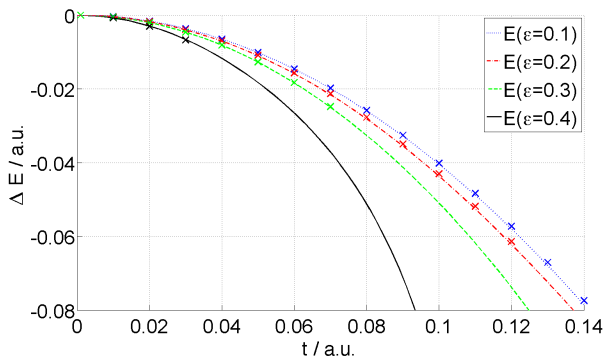


FIG. 13: Energies of a 1-dimensional system with disorder parameters $\epsilon = 0.1$ (blue dotted line), $\epsilon = 0.2$ (red dashed-dotted line), $\epsilon = 0.3$ (green dashed line) and $\epsilon = 0.4$ (black solid line) compared to results obtained with VCA⁸, which are marked with \times .

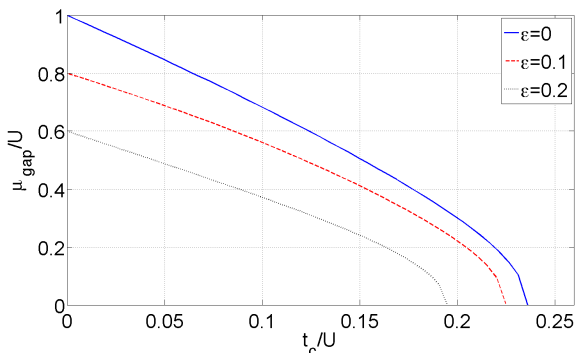


FIG. 14: The Mott insulator gap as function of the critical hopping strength for a 2-dimensional system with zero disorder, a system with $\epsilon = 0.1$ and for a system with $\epsilon = 0.2$.

obtained with VCA⁸. Energy corrections were included up to 7th order (8th order for the ordered system) and we averaged over 500 configurations. The solid lines are our results calculated with the Kato-Bloch algorithm and the \times mark the results from VCA.

As before, our results are in excellent agreement with those computed with VCA, which can be seen especially well for the $\epsilon = 0.1$ and $\epsilon = 0.2$ cases. Unfortunately we don't have data from VCA for $\epsilon = 0.3$ and $\epsilon = 0.4$ at higher hopping parameters, so the possibilities to compare these two methods for these parameters are rather little. The data at low hopping strength and the general information gathered up to this point however suggest a good agreement of Kato-Bloch and VCA nevertheless.

In Fig. 14 we plotted the width of the Mott insulator regions as function of the critical hopping strength t^* . The blue solid line stands for the ordered system, the red one for the system with $\epsilon = 0.1$ and the black one for $\epsilon = 0.2$.

VI. THE JAYNES-CUMMINGS LATTICE MODEL

The JCL model is an enhancement of the Rabi model³³. While the semi-classical Rabi model considers a two-level atomic system that is disturbed by an electromagnetic field, the JCL model takes these thoughts further and describes a two-level atomic system that interacts with quantized modes of light.

The JCL model is very important for quantum physics, as it describes atoms coupled to cavity modes, therefore being a way to realize quantum-bits and -computing. The following short explanation follows strongly the approach of ref.³⁴ and all quantities are expressed in units of \hbar .

The hamiltonian of a JC system consists of three parts, an atom part $\hat{H}_a = \epsilon |\uparrow\rangle \langle \uparrow|$ which assigns the energy ϵ to the excited atom states, a cavity part $\hat{H}_c = \omega_c \hat{a}_i^\dagger \hat{a}_i$ counting the bosons in the cavity and appointing them the energy ω_c and a part that describes the coupling between atom and cavity \hat{H}_{ac} , which can be written like

$$\hat{H}_{ac} = -\frac{1}{\hbar} \hat{\mathbf{d}} \cdot \hat{\mathbf{E}}_c. \quad (31)$$

With the expression for the quantum mechanical dipole operator $\hat{\mathbf{d}} = \mathbf{d}(\mathbf{e}_a \sigma_- + \mathbf{e}_a^* \sigma_+)$ and the cavity field operator $\hat{\mathbf{E}}_c = \mathcal{E}_0(\mathbf{e}_c \hat{\mathbf{a}} + \mathbf{e}_c^* \hat{\mathbf{a}}^\dagger)$ this becomes

$$\hat{H}_{ac} = -\frac{d}{\hbar} (\mathbf{e}_a \sigma_- + \mathbf{e}_a^* \sigma_+) \cdot \mathcal{E}_0 (\mathbf{e}_c \hat{\mathbf{a}} + \mathbf{e}_c^* \hat{\mathbf{a}}^\dagger). \quad (32)$$

Here, \hat{a} and \hat{a}^\dagger are again the bosonic annihilation and creation operators for the cavity modes, σ_+ and σ_- are the atomic raising and lowering operators that raise a ground state atom to its excited state and vice versa. \mathbf{e}_a and \mathbf{e}_c are vectors describing the field polarization in the atom or the cavity system and \mathcal{E}_0 is a normalization factor. Usually there is also a factor $f(r)$ present, which describes the spatial configuration of the field mode, but for sake of simplicity it is set to unity here.

If we get rid of the braces in Eq. (32), we are left with four terms. The term with $\sigma_- \hat{a}$ stands for the process where the excited atom relaxes to its ground state while a photon is annihilated. The $\sigma_+ \hat{a}^\dagger$ term describes the opposite effect, i.e. the atom is shifted to the higher state and a photon is created. In our case, where the resonance frequencies of the atom and the cavity are very close to each other, these two effects play a very minor role and are therefore omitted from this point on.

The two much more important terms are those with $\sigma_- \hat{a}^\dagger$ and $\sigma_+ \hat{a}$. The first one explains the emission of a photon when the atom relaxes to its lower state and the second one translates to an excitation of the atom when absorbing a photon. Hence, our simplified hamiltonian \hat{H}_{ac} has the form

$$\hat{H}_{ac} = -\frac{\Omega}{2} (\sigma_+ \hat{a} + \sigma_- \hat{a}^\dagger), \quad (33)$$

with the Rabi frequency Ω

$$\Omega = 2 \frac{d\mathcal{E}_0 \mathbf{e}_a^* \mathbf{e}_c}{\hbar}. \quad (34)$$

This frequency is a measurement for the strength of the coupling of the two systems. The eigenstates of the atom hamiltonian \hat{H}_a are $|\downarrow\rangle$, $|\uparrow\rangle$, the first denoting the ground state, the second the excited state. On the other hand, the cavity hamiltonian \hat{H}_c has the eigenstates $|g\rangle$, the already known Fock-states from Sec. II. Therefor, the eigenstates of the uncoupled system will be the tensor products $|g, \downarrow\rangle$ and $|g, \uparrow\rangle$.

If the detuning of the system $\Delta = \omega_c - \epsilon$ is zero or very small compared to ω_c , the states with the same particle number, i.e. $|g, \downarrow\rangle$ and $|g-1, \uparrow\rangle$ are degenerated or nearly degenerated respectively. The complete energy of a system with g particles is therefor saved in a state with g photons and no atom excitations $|g, \downarrow\rangle$, or a state with $g-1$ photons and one atom excitation $|g-1, \uparrow\rangle$. (The exception being a system with no particles, which of course can only be described by $|0, \downarrow\rangle$.) The coupling hamiltonian \hat{H}_{ac} only translates between those states with the same particle number.

We are therefor dealing with a two-level system, hence the operators σ_+ and σ_- can be computed using the Pauli matrices, i.e. $\sigma_{\pm} = \sigma_x \pm i\sigma_y$. With this we can write down a matrix equation for the dimensionless hamiltonian of the complete system with n particles³⁵:

$$H_{JC}^{(n)} = \begin{pmatrix} (g-1)\omega_c + \epsilon & \frac{\Omega}{2}\sqrt{g} \\ \frac{\Omega}{2}\sqrt{g} & g\omega_c \end{pmatrix} \quad (35)$$

The energy eigenvalue can then be expressed like

$$E_{g,\pm} = g\omega_c - \frac{\Delta}{2} \pm q(g), \quad (36)$$

with

$$q(g) = \sqrt{\left(\frac{\Delta}{2}\right)^2 + g\left(\frac{\Omega}{2}\right)^2}. \quad (37)$$

The \pm -sign refers to the sign of $|g, -\rangle$ and $|g, +\rangle$, introduced in Eq. (38) and (39). If there are no particles in the system, there is just one state possible, $|0, \downarrow\rangle$. The energy eigenvalue for this case is $E_{g=0} = 0$.

The eigenstates corresponding to the energies of Eq. (36) are

$$|g, -\rangle = \cos \Theta_g |g-1, \uparrow\rangle - \sin \Theta_g |g, \downarrow\rangle \quad (38)$$

$$|g, +\rangle = \sin \Theta_g |g-1, \uparrow\rangle + \cos \Theta_g |g, \downarrow\rangle, \quad (39)$$

where we used the short notations

$$\sin \Theta_g = \sqrt{\frac{q(g) - \frac{\Delta}{2}}{2q(g)}} \quad \text{and} \quad \cos \Theta_g = \sqrt{\frac{q(g) + \frac{\Delta}{2}}{2q(g)}}. \quad (40)$$

The states (38) and (39) are linear combinations of the two possible states with the same total particle number. As $|g, -\rangle$ corresponds to the lower energy, it is the ground state of our system while $|g, +\rangle$ is the excited state with the higher total energy. We are talking here about the atom-cavity system as a whole, so the ground state $|g, -\rangle$ should not be confused with the atom ground state $|\downarrow\rangle$.

Recapitalizing, the final JC hamiltonian for an atom-cavity system looks as follows:

$$\begin{aligned} \hat{H}_{JC} = & \omega_c \hat{a}^\dagger \hat{a} + \epsilon |\uparrow\rangle \langle \uparrow| \frac{\Omega}{2} (\hat{a} |\uparrow\rangle \langle \downarrow| + \hat{a}^\dagger |\downarrow\rangle \langle \uparrow|) \\ & - \mu (\hat{a}^\dagger \hat{a} + |\uparrow\rangle \langle \uparrow|) \end{aligned} \quad (41)$$

Additionally to what was said in the previous paragraphs, an atom-cavity site may also have an additional energy that is dependent on the total particle number, due to a chemical potential μ , which is considered with the last term in our JC hamiltonian.

A. Changes in the algorithms

In Sec. VI we took a look at the hamiltonian of a single atom-cavity site. Now we are going to construct a regular lattice by arranging a large array of such sites and allow the bosons to tunnel to neighboring sites with tunneling strength t . The JC hamiltonian of a single site $\hat{H}_{JC,i}$ is given in Eq. (41) and the 'hopping' hamiltonian is the same as for the BH model (see Sec. II)

$$\hat{H}_{JCL} = \sum_i \hat{H}_{JCL,i} + \hat{H}_{hop}. \quad (42)$$

The JC site hamiltonian \hat{H}_{JC} does not alter the particle number of the eigenstates, but the hopping hamiltonian \hat{H}_{hop} does. It is therefor clear, that the hopping term is again the perturbative part.

The fact, that there are two eigenstates of the JC model now belonging to the same particle number g involves a disadvantage. As we know, the term S_k of our Kato formula projects the current state to the according eigenstate of \hat{H}_0 . The current state will therefor either be projected onto $|g, -\rangle$ or $|g, +\rangle$. This means, that one has to add the information in which eigenstate we are projecting, i.e. $S_k \rightarrow S_{k,\sigma}$ with σ indicating which eigenstate we should take.

$$S_{k,\pm} = \begin{cases} -|g, -\rangle \langle g, -| & \text{for } k=0 \\ \sum_{|i,\pm\rangle \neq |g,-\rangle} \frac{|i,\pm\rangle \langle i,\pm|}{(E_{g,-}^{(0)} - E_{i,\pm}^{(0)})^k} & \text{otherwise} \end{cases} \quad (43)$$

In order to calculate the energy correctly, we also have to consider not only every possible sequence $\{k_\nu\}^{(n-1)}$ but also every possible permutation of the signs $\{\sigma_\nu\}^{(n-1)}$.

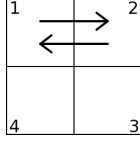


FIG. 15: One possible path in second order.

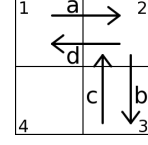


FIG. 17: One possible path in fourth order.

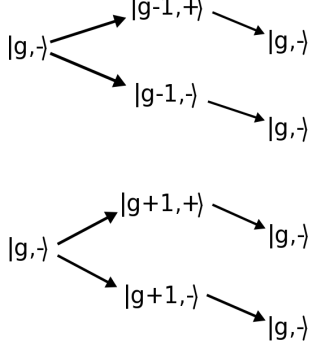


FIG. 16: All possible sequences of the path in Fig. 15.

Our equation for the complete energy correction of n^{th} order therefor reads

$$\Delta E_g^{(n)} = \sum_{\{\sigma_\nu\}^{(n-1)}} \Delta E_{g,\sigma_\nu}^{(n)}, \quad (44)$$

In order to deduce the right σ_ν sequences we will take a look at a few different paths. Let's consider the most simple path there is, depicted in Fig. 15 appearing in the second order energy correction:

After the first hop from site 1 to site 2, we do have $g-1$ particles at site 1. But the state of this site could have either been projected to $|g-1,-\rangle$ or $|g-1,+\rangle$. An exception would of course be, if there were $g=1$ particles at each site before the hopping, in which case only the $|0,\downarrow\rangle$ state would be possible for site 1 after the first hopping. We will from now on omit mentioning this exception as it always results in the same state.

Site 2 contains $g+1$ particles after the first tunneling and will be projected in either the $|g+1,-\rangle$ or the $|g+1,+\rangle$ state. After the second hopping takes place, both sites are again populated by g particles and at each site the ground state $|g,-\rangle$ has to be present in order to lead to a non-vanishing energy contribution. A graphical depiction of this can be seen in Fig. 16.

To calculate the energy contribution of this path correctly, we would now have to calculate the energy of each of the 4 possible sequences and sum them up.

In order to get the right number of sequences, we have to include information about the number of nodal points, i.e. how many times the ground state is restored before the whole perturbation process is finished. This is shown in Fig. 17 and Fig. 19. While both of these figures show the same diagram, the order of hoppings is different. In Fig. 17 the ground state is never present up until the very end resulting in the sequences of Fig. 18. The path

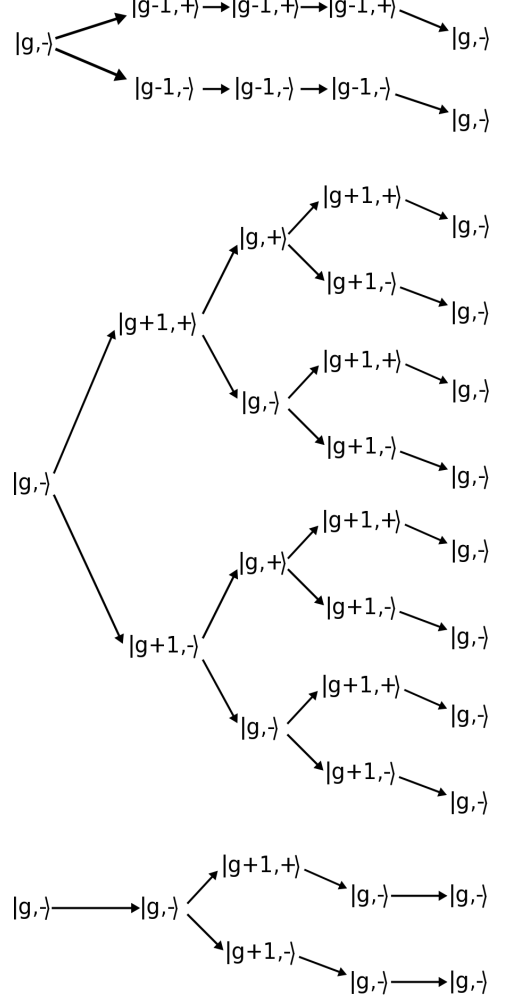


FIG. 18: All possible sequences of the path in Fig. 17

in Fig. 19 however restores the ground state after two hopping processes, leading to the sequences of Fig. 20.

To compute the total numbers of sequences for a certain path, we count the number of arrows pointing to a site $N_{a,i}$. For closed paths this number has to be of course the same as the number of arrows pointing away from a site,

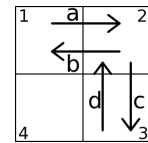


FIG. 19: One possible path in fourth order.

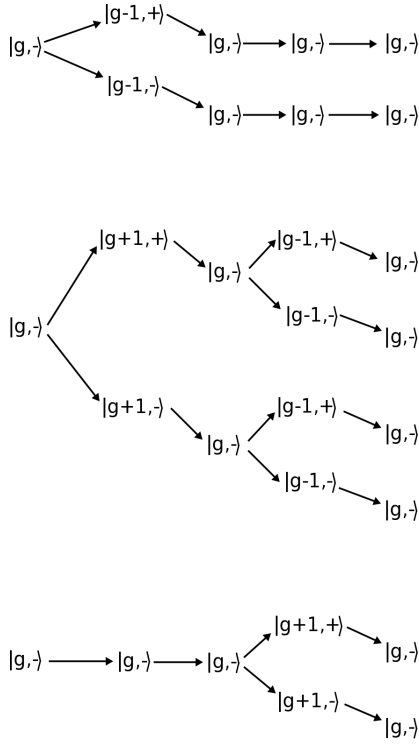


FIG. 20: All possible sequences of the path Fig. 19

the number of bonds of site i is therefore $N_{B,i} = 2N_{a,i}$. Additionally, we need to know the number of nodal points $N_{n,i}$ for this site. The number of sequences $N_{seq,i}$ for site i is then

$$N_{seq,i} = 2^{N_{B,i} - (N_{n,i} + 1)} \quad (45)$$

and the total number of sequences N_S is therefore the product of these $N_{S,i}$

$$N_{seq} = \prod_i N_{seq,i} . \quad (46)$$

The number of bonds for a specific site can be determined very easily with the aid of adjacency matrices. As we know, the i^{th} row tells us, to which sites particles hop originating from site i . The i^{th} column on the other hand contains the information from which sites arrows point to site i . The adjacency matrix for the path shown in Fig. 17 for example is

$$M = \begin{pmatrix} 0 & 1 & 0 \\ 1 & 0 & 1 \\ 0 & 1 & 0 \end{pmatrix} . \quad (47)$$

The vector v_B resulting when summing over all columns of the matrix stated by equation (47) reads $v_B^T = (1, 2, 1)$. Doubling it gives us $(2, 4, 2)$, which means that there are two bonds at site 1, four bonds at site 2 and again two bonds at site 3.

TABLE II: Computation times in seconds for the JCL energy correction up to order $\nu = 6$ for different filling factors g and dimensions d .

| ν | $g = 1$ | | | $g = 2$ | | |
|-------|---------|---------|---------|---------|---------|---------|
| | $d = 1$ | $d = 2$ | $d = 3$ | $d = 1$ | $d = 2$ | $d = 3$ |
| 2 | 0, 25 | 0, 24 | 0, 35 | 0, 23 | 0, 22 | 0, 32 |
| 4 | 0, 37 | 0, 46 | 0, 53 | 0, 58 | 0, 72 | 0, 75 |
| 6 | 8, 30 | 27, 15 | 27, 71 | 58, 61 | 153, 06 | 156, 54 |

With all that in mind we can reuse most of the algorithms created for the energy calculations of the BH model. The path creation and the reduction to topologically unique diagrams can be copied without any change. The algorithm for the energy calculation however has to be adopted at the point where all the permutations of a diagram are created. At this point we have to compute the adjacency matrix for every permutation to determine the number of bonds for each site. With this information we can create the allowed σ -sequences for each permutation individually, calculate the energy for every sequence and sum them up. After all σ -sequences have been worked off, we proceed to the next permutation.

B. Results

The additional summation over all σ -sequences of course slows down the energy computation compared to the calculations for the BH model, but the computation times up to order 6 are still in the range of seconds, as table II shows.

All systems we are going to discuss have in common that we have chosen the parameter $\Omega = 0$ and we have also set the detuning $\Delta = 0$. A more detailed look at different sets of parameters can be found in ref.³⁶.

In Fig. 21 one can see the high quality of the data achieved. It shows the computed energy correction of a 2-dimensional system with filling factor $g = 1$, but for different orders of correction. The solid (blue) line contains only the second order energy correction $\Delta E^{(2)}$, the dashed (red) line results from combining the second order and fourth order corrections, the dashed-dotted (green) line shows the energy correction up to sixth order and the dotted (black) line up to the eighth order.

One can see, that while the solid (blue) line differs from the others quite significantly, the dashed and dotted lines are very close to each other. In fact, the lines for the 6th and 8th order lie on top of each other perfectly at this scale, suggesting a very high fidelity already for the sixth order correction.

Additionally, Fig. 22 shows a comparison of data computed with VCA¹⁰. Two systems were simulated, with

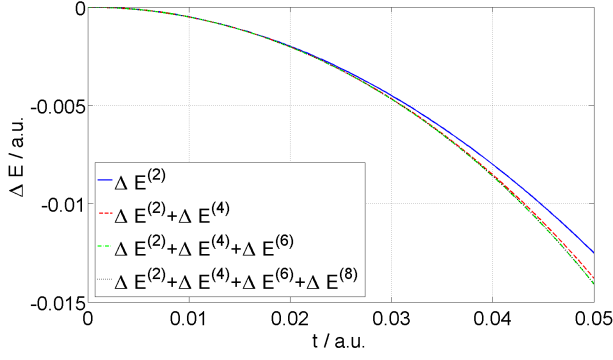


FIG. 21: Comparing the fidelity of the computed energy corrections depending on the orders of correction included for a JCL system with 2 dimensions and unity filling factor.

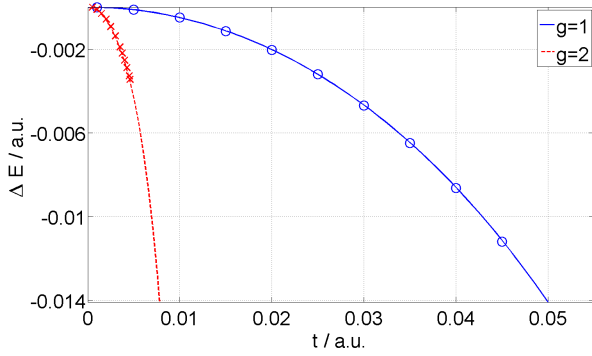


FIG. 22: Comparison of calculations carried out with the Kato-Bloch algorithm (solid and dashed lines) and with VCA¹⁰ (circles and \times) of two systems with dimension $d = 2$ but different filling factors g .

the first having 2 dimensions and unity filling factor and the second also 2 dimensions but filling factor $g = 2$.

The solid and the dashed lines represent the results obtained with the Kato-Bloch approach and the circles and \times those from VCA. As previously with the BH system (see Fig. 6 in Sec. III C), our results are in excellent agreement with VCA.

A comparison of the energy of different systems can be seen in Fig. 23. Simulated were systems with 1, 2 and 3 dimensions and with the filling factors $g = 1$ and $g = 2$. It is worthwhile to note, that the energies of systems with different g differ more than for systems with different dimensions d .

Next we move on to the Mott insulator-superfluid phase transition calculations for the JCL model.

C. The Mott Insulator-Superfluid Phase Transition

The same changes in the algorithm that have been discussed in the previous chapter have also to be taken into account if one wants to determine the Mott insulator-

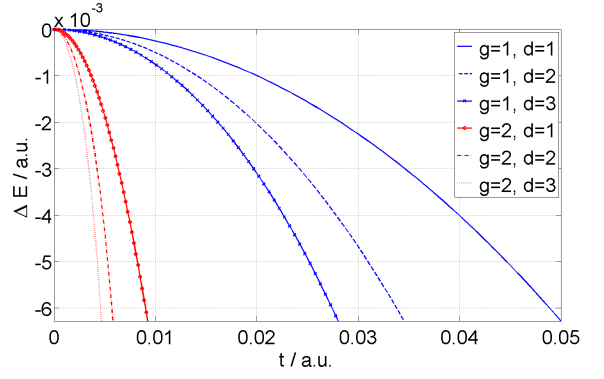


FIG. 23: Comparison of the energies of systems with various filling factors g and dimensions d as a function of the hopping strength t .

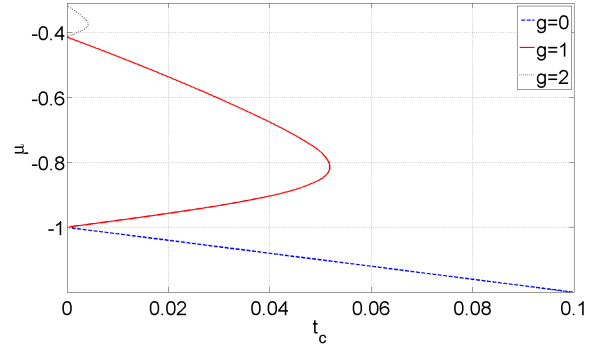


FIG. 24: The Mott insulator-superfluid phase boundary for a system with 2 dimensions, $\Delta = 0$, $\Omega = 0$ and filling factors $g = 0$ (dashed), 1 (solid) and 2 (dotted).

superfluid phase boundary for the JCL model. But furthermore it is no longer necessarily true that the number of arrows pointing from a site is the same as the number of arrows pointing away from it. This little inconvenience is taken care of by just computing the sum along the rows and the sum along the columns of the adjacency matrix and adding these vectors point-wise, thereby getting the number of bonds per site.

With that in mind we can simply take the Mott insulator-superfluid algorithm of the BH model and apply the same changes to the c_2 computation part as we applied to the energy correction algorithm in order to calculate the energy of the JCL model instead of the BH model.

Fig. 24 shows the Mott insulator-superfluid phase boundary for a 2-dimensional system with different filling factors $g = 0$ (dashed), $g = 1$ (solid) and $g = 2$ (dotted). The area that is confined by the dashed (blue) line is the Mott insulator phase with a filling factor $g = 0$. Analogously, the solid (red) line limits the Mott insulator phase with $g = 1$ and the dotted (black) line the Mott insulator phase with $g = 2$.

The same set of parameters we used in Fig. 24 has been used to determine the phase boundary for a 3-

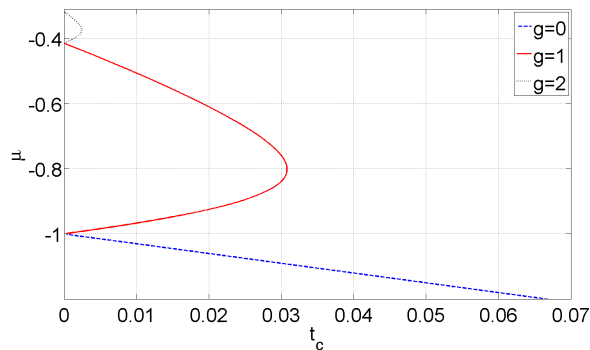


FIG. 25: The Mott insulator-superfluid phase boundary for a system with 3 dimensions, $\Delta = 0$, $\Omega = 0$ and filling factors $g = 0$ (dashed), 1 (solid) and 2 (dotted).

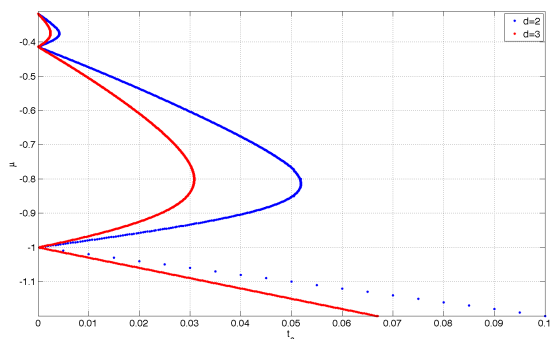


FIG. 26: The Mott insulator-superfluid phase boundary for systems with 2 and 3 dimensions, $\Delta = 0$, $\Omega = 0$ and filling factors $g = (1, 2, 3)$.

dimensional system as depicted in Fig. 25.

It is of interest to note that the point, where $t^* = 0$, is independent of the dimension of the system and can be calculated easily with $\sqrt{g} - \sqrt{g+1}$ (see ref.³⁶). As one can see, this coincides perfectly with our calculations.

As was the case with the the BH model, the phase boundary for 1-dimensional systems has to be calculated by the use of 'defect' particles already explained in Sec. IV A.

VII. CONCLUSION AND OUTLOOK

In this work, we incorporated the Kato-Bloch perturbation approach to calculate the ground state energies

and Mott insulator-superfluid phase boundaries for various BH and JCL systems. The Kato-Bloch approach leads to explicit formulas for any perturbation order, i.e. there is a clear distinction of the orders in contrast to the mixed expressions in the Schrödinger-Rayleigh perturbation theory. Moreover, all the appearing expressions can be represented diagrammatically, which allows to utilize knowledge from graph theory to speed up the numerical algorithms considerably. In fact we were able to perform all calculations on an off-the-shelf computer in appropriate time.

Additionally to these advantages, the comparison of our results with those from other methods, including DMRG and VCA prove the high accuracy of our implementation. Building upon the work by Teichmann et al.², who dealt with the ground state energy, the Mott insulator-superfluid phase diagram and other quantities for the BH system in detail, we focused on adding disorder to the BH model, applying this approach to the JCL model and on solving the problem that appears when trying to calculate the phase boundary for 1-dimensional systems with the method of effective potential.

The Kato-Bloch approach is an extremely powerful method and could be easily generalized to deal with other lattice systems apart from the BH and the JCL as well. Especially interesting in our eyes would be the implementation of models with nearest neighbor interaction or an additional superlattice structure, which exhibit a richer phase diagram as the BH and the JCL model.

Acknowledgments

The authors want to thank N. Teichmann for providing their process chain approach data to countercheck our results. We also want to thank H. Monien for allowing us to use their DMRG results to compare with ours. Last but not least we want to thank E. Arrigoni and M. Knap for many fruitful discussions on this topic. This work was partly supported by the Austrian Science Fund (FWF P18551-N16)

* cheil@sbox.tugraz.at

¹ A. Eckardt, Phys. Rev. B **79**, 195131 (2009).

² N. Teichmann, D. Hinrichs, M. Holthaus, and A. Eckardt, Phys. Rev. B **79**, 224515 (2009).

³ I. Bloch and W. Zwerger, Rev. Mod. Phys. **80**, 885 (2008), ISSN 0034-6861.

⁴ M. Greiner, O. Mandel, T. Esslinger, T. W. Hansch, and I. Bloch, Nature **415**, 39 (2002), ISSN 0028-0836.

⁵ S. Sachdev, *Quantum Phase Transitions* (Cambridge University Press, 2001), ISBN 0521004543.

⁶ D. Jaksch, C. Bruder, J. I. Cirac, C. W. Gardiner, and P. Zoller, Phys. Rev. Lett. **81**, 3108 (1998).

- ⁷ M. P. A. Fisher, P. B. Weichman, G. Grinstein, and D. S. Fisher, Phys. Rev. B **40**, 546 (1989).
- ⁸ M. Knap, E. Arrigoni, and W. von der Linden, Phys. Rev. B **81**, 235122 (2010).
- ⁹ T. D. Kühner, S. R. White, and H. Monien, Phys. Rev. B **61**, 12474 (2000).
- ¹⁰ M. Knap, E. Arrigoni, and W. von der Linden, Comp. Phys. Comm. **online** (2011), ISSN 0010-4655.
- ¹¹ M. P. A. Fisher, P. B. Weichman, G. Grinstein, and D. S. Fisher, Phys. Rev. B **40**, 546 (1989).
- ¹² T. D. Kühner and H. Monien, Phys. Rev. B **58**, R14741 (1998).
- ¹³ S. Rapsch, U. Schollwöck, and W. Zwerger, Europhys. Lett. **46**, 6 (1999).
- ¹⁴ C. Kollath, U. Schollwöck, J. von Delft, and W. Zwerger, Phys. Rev. A **69**, 031601 (2004).
- ¹⁵ C. Kollath, A. M. Läuchli, and E. Altman, Phys. Rev. Lett. **98**, 180601 (2007).
- ¹⁶ G. G. Batrouni and R. T. Scalettar, Phys. Rev. B **46**, 9051 (1992).
- ¹⁷ S. Wessel, F. Alet, M. Troyer, and G. G. Batrouni, Phys. Rev. A **70**, 053615 (2004).
- ¹⁸ B. Capogrosso-Sansone, N. V. Prokofév, and B. V. Svistunov, Phys. Rev. B **75**, 134302 (2007).
- ¹⁹ B. Capogrosso-Sansone, S. G. Söyler, N. Prokofév, and B. Svistunov, Phys. Rev. A **77**, 015602 (2008).
- ²⁰ J. K. Freericks and H. Monien, Phys. Rev. B **53**, 2691 (1996).
- ²¹ N. Elstner and H. Monien, Phys. Rev. B **59**, 12184 (1999).
- ²² T. Kato, Prog. Theor. Phys. **4**, 514 (1950), ISSN 0033-068X.
- ²³ M. P. Gelfand, R. R. P. Singh, and D. A. Huse, J. Stat. Phys. **59**, 1093 (1990), ISSN 0022-4715.
- ²⁴ A. Messiah, *Quantum Mechanics* (Dover Publications, 1999), ISBN 0486409244.
- ²⁵ A. Gibbons, *Algorithmic Graph Theory* (Cambridge University Press, 1985), ISBN 9780521288811.
- ²⁶ J. W. Negele and H. Orland, *Quantum Many-Particle Systems* (Perseus Books (Sd), 1988), ISBN 0201125935.
- ²⁷ F. E. A. dos Santos and A. Pelster, Phys. Rev. A **79**, 013614 (2009).
- ²⁸ E. T. Whittaker and G. N. Watson, *A Course of Modern Analysis* (Cambridge University Press, 1927), 4th ed., ISBN 0521091896.
- ²⁹ J. K. Freericks and H. Monien, Phys. Rev. B **53**, 2691 (1996).
- ³⁰ M. Knap, E. Arrigoni, and W. von der Linden, Phys. Rev. B **81**, 024301 (2010).
- ³¹ G. H. Hardy, *Divergent Series* (American Mathematical Society, 2000), 2nd ed., ISBN 0821826492.
- ³² G. A. B. Jr and P. Graves-Morris, *Pad Approximants* (Cambridge University Press, 1996), 2nd ed., ISBN 9780521450072.
- ³³ E. T. Jaynes and F. Cummings, Proc. IEEE **51**, 89 (1963), ISSN 0018-9219.
- ³⁴ S. Haroche, J. Raimond, and S. Haroche, *Exploring the Quantum: Atoms, Cavities, and Photons* (Oxford University Press, 2006), ISBN 0198509146.
- ³⁵ V. Hussin and L. M. Nieto, J. Math. Phys. **46**, 122102 (2005), ISSN 00222488.
- ³⁶ J. Koch and K. L. Hur, Phys. Rev. A **80** (2009), ISSN 1050-2947.